A Ring-Based 25 Gb/s DAC-Less PAM-4 Modulator

Mohammed Shafiqul Hai, Monireh Moayedi Pour Fard, and Odile Liboiron-Ladouceur, *Senior Member, IEEE*

***Abstract*—A novel PAM-4 12.5 Gbaud/s inter-coupling modulator based on a Mach–Zehnder interferometer assisted ring resonator is demonstrated. The 25 Gb/s PAM-4 optical signal is generated by driving the modulator with two independent electrical signals with an amplitude of 3 V_{pp} at 2 V reverse bias. Reverse bias operation mode of the modulator enables achieving an electro-optic (EO) bandwidth of approximately 14 GHz without preemphasis of the electrical driving signals or equalization techniques. This configuration successfully simplifies the operation of the modulator in generating PAM-4 signals without the need for a digital-to-analog converter (DAC). Experimental results show proper generation of a PRBS data stream. The proposed modulator has a compact footprint of 0.48 mm^2 with a bandwidth density of 52.08 Gb/s/mm^2.**

***Index Terms*—Optical interconnects, optical modulators, PAM-4 modulators, ring resonators, silicon photonics.**

I. Introduction

INTENSITY-modulated/direct-detection (IM/DD) based optical communication link is a promising low-cost solution to build 100 Gb/s/λ data rate for short reach (200 m to 2 km) interconnects between data centers [1]. Advanced modulation format based Mach-Zehnder modulator (MZM) on silicon photonic platform offers the possibility of designing power efficient, low-cost and integrated IM/DD networks. The linear phase shift with an applied reverse bias voltage and long electrode structure of the MZMs facilitates the design of segmented electrode based PAM-4 (two segment electrode) or PAM-16 (four segment electrode) modulators [2]. However, to reduce the driving voltage amplitude and footprint of the transmitter, researchers are also investigating the operation principle of resonance based modulators (i.e., ring modulators [3] or MZI assisted ring modulators [4]) to generate PAM-4 modulation format signal. It remains challenging to design multiple segment electrode structure on the small perimeter of ring modulator (e.g., 50 μm ring perimeter in [3]). For example, to circumvent the ring small radius in [3], a single electrode ring modulator generates 60 Gb/s (30 GBaud/s) PAM-4 optical signal. The PAM-4 electrical signal is initially generated using a three bit digital-to-analog converter (DAC).

To reduce the cost and power consumption by eliminating the DAC stage in generating PAM-4 signal with the ring-based modulator, we proposed a MZI assisted ring modulator in [4] where a two-segment electrode is designed in the ring cavity. This configuration facilitates the generation of the PAM-4 format optical signal as the modulator is driven by two independent electrical signals (most significant bit, (MSB), and least significant bit, (LSB)). In [4], the intra-cavity modulation is achieved by forward biasing the p-n diode electrode segments limiting the data rate of the fabricated PAM-4 modulation to 120 MBaud/s. In an intra-cavity based ring modulator, extinction ratio of the transmission response changes due to the spectral shift of the resonance with the applied electrical voltage. This creates a nonlinear relation between the extinction ratio and applied electrical voltage. Therefore, generating the PAM-4 signal by driving the multi-segmented electrodes in an intra-cavity based ring modulator depends on fabrication tolerance. An MZI assisted ring resonator modulator was proposed in [5] where a forward biased inter-coupling structure achieved 28 Gb/s on-off keying (OOK or PAM-2) modulation using a pre-emphasized push-pull electrical driving signal. Pre-emphasis in the electrical driving signal overcomes the slow carrier injection rate in forward bias mode enabling higher data rate [6]. In a pre-emphasized electrical signal, higher voltage is applied to the forward biased p-n diode during the first fraction of a bit duration for a digital one to enable faster transition from '0' to '1' or '1' to '0' [6]. In [7], a theoretical model of a PAM-4 inter-coupling ring modulator is proposed with two design approaches where the electrode lengths were varied to drive the modulator in forward or reverse bias mode. In the inter-coupling modulator, the extinction ratio of the optical spectrum at the critical coupling point decreases with the applied electrical voltage. This facilitates achieving more than two optical power levels (i.e., four optical power levels in the case of PAM-4 modulation) using multi-segmented electrodes. Further, we found that for high-speed operation in the forward bias mode, the PAM-4 modulation requires two pre-emphasized electrical signals, which increases the operational complexity of the modulator. One of the pre-emphasized electrical signal diminishes the amplitude difference between the two intermediate levels of the PAM-4 signal leading to unequal differences between the four levels of the PAM-4 signal. Thus, driving the ring modulator in reverse bias mode leads to a more practical design where two conventional OOK electrical signals can generate high data rate PAM-4 signal.

In this work, we present the first experimental demonstration of a reverse biased MZI assisted ring modulator, where two p-n diode electrode segments are designed on the MZI arm for inter-coupling modulation. The phase of the two independent electrical driving signals are adjusted such that a 12.5 Gbaud/s PAM-4 signal is achieved at the output. We have also included a heater layer on top of the coupler arm to tune the coupling ratio of the modulator such that larger extinction ratio is achieved in the presence of thermal or fabrication variations. The paper is organized in five sections. In Section II, an overview of

Manuscript received January 31, 2016; revised May 18, 2016; accepted June 18, 2016. Date of publication July 9, 2016; date of current version September 12, 2016. This work is part of the SPEED research project (Silicon Photonic Electrically Engineered Devices) and was supported by NSERC (RDCPJ438811-12), PROMPT (PJT-2011-17), and Ciena Corporation.

Mohammed Shafiqul Hai and Monireh Moayedi Pour Fard contributed equally to this work.

The authors are with the Electrical and Computer Engineering Department, McGill University, Montreal, QC H3A 0G4, Canada (e-mail: md.hai@mail.mcgill.ca).

Color versions of one or more of the figures in this paper are available online at http://ieeexplore.ieee.org.

Digital Object Identifier 10.1109/JSTQE.2016.2584978

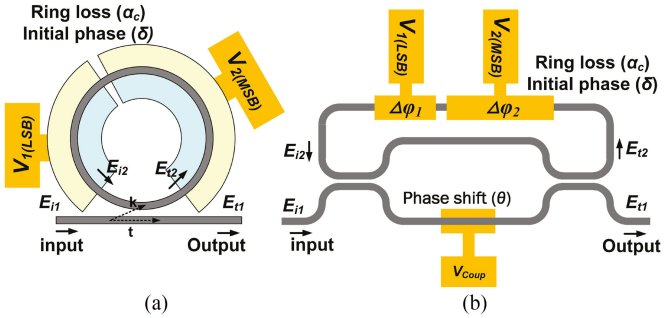

Fig. 1. Multi-segmented intra-cavity PAM-4 modulator (a) with directional coupler, (b) with an MZI as a tunable coupler.

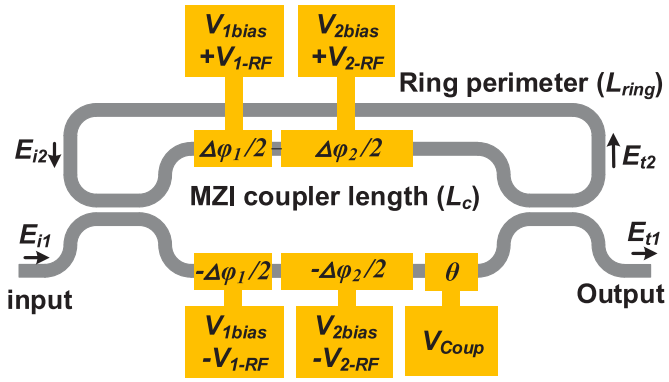

Fig. 2. Multi-segmented inter-coupling PAM-4 modulator with push–pull configuration.

ring-based PAM-4 modulators is presented. The design and simulation results of the proposed inter-coupling PAM-4 modulator are discussed in Section III. Section IV presents the experimental results of the fabricated modulator. Finally, the conclusion is presented in Section V.

II. Ring-Based PAM-4 Modulator

In this section, we first describe two types of ring based PAM-4 modulators and present the analytical equations used towards the design of the proposed ring-based 25 Gb/s PAM-4 modulator.

A. Multi-Segmented Intra-Cavity PAM-4 Modulator

The schematic of the multi-segmented intra-cavity PAM-4 modulator is shown in Fig. 1. Fig. 1(a) illustrates the modulator with a directional coupler. In Fig. 1(b), the directional coupler is replaced by a Mach-Zehnder Interferometer (MZI) enabling tunable coupling between the waveguide and the ring. Using a tunable coupler adds a degree of freedom in controlling the extinction ratio and the resonance linewidth to achieve four optical signal levels at the output of the modulator [4]. Modulation in the intra-cavity modulator is generated by the cavity round-trip phase shift, $\Delta\phi$, and/or slight variation of the cavity loss, α_c, while the optical field coupled to the cavity is fixed. The bandwidth of the intra-cavity modulator can be limited by the photon lifetime which is related to the resonance linewidth of the ring cavity. This limitation can be overcome by modulating the amount of light coupled to the ring cavity using a modulation configuration referred as inter-coupling modulation [8] discussed in the next section.

The total phase shift in the PAM-4 modulator is $\Delta\phi = \Delta\phi_1 + \Delta\phi_2$ (Fig. 1) generated by applying an electrical driving signal V_1 ($V_1 = V_{1\text{bias}} \pm V_{1-\text{RF}}$) to the shortest diode segment and V_2 ($V_2 = V_{2\text{bias}} \pm V_{2-\text{RF}}$) to the longest diode segment. Similar to an electrical DAC, it is desirable that for generating the multi-level output signal, the two binary signals V_1 and V_2 have the same DC (V_{bias}) and AC (V_{RF}) values. Hence, the length of the phase shifters should be proportional to the required phase shift for the LSB and the MSB of the generated output symbol. In the multi-segmented PAM-4 MZI modulator presented in [2], the two segments are selected binary weighted ($L_{\text{MSB}} = 2 \times L_{\text{LSB}}$). Due to the nonlinear nature of the ring-based modulator transfer function, however, the ratio of the longer to the shorter p-n diode segment is not binary weighted and needs to be determined through simulation.

B. Multi-Segmented Inter-Coupling PAM-4 Modulator

By replacing the directional coupler with a MZI based coupler in the ring cavity, we can also modulate the amount of light coupled to the ring cavity by changing the total phase shift $\Delta\phi = \Delta\phi_1 + \Delta\phi_2$ between the two arms of the MZI. This modulator is known as an inter–coupling modulator [7]. Fig. 2 shows the schematic of the inter-coupling PAM-4 modulator with push–pull electrical driving signal. The advantage of driving the MZI arms in a push–pull scheme is that the resonance wavelength of the ring cavity does not shift with the applied electrical diving signals and hence demonstrate zero chirp operation. Further, the bandwidth of the device is no longer limited by the narrow resonance linewidth [5].

The design flow of the inter-coupling PAM-4 modulator with push–pull driving signal is presented in [7] where it was assumed that the MZI is lossless. In practice, the losses in the MZI arms cannot be ignored as their lengths are in the same order as the cavity feedback length. Furthermore, the voltage-dependent free carriers of the p-n junction increase the waveguide loss in the fabricated device, which must be considered in designing the device. The required symmetry for the two MZI arms, especially in push–pull drive PAM-4 modulator, makes the device sensitive to fabrication variations leading to complex voltage settings for the fabricated device.

III. Design and Simulation of the Proposed Modulator

In this section, we first present the proposed inter-coupling PAM-4 modulator. Next, we describe the simulation methodology and design parameter followed by simulation results of the proposed modulator. The inter-coupling PAM-4 modulator can be driven with single ended electrical signals reducing the complexity of the voltage settings (Fig. 3). It is this proposed configuration that is designed, fabricated, and discussed in this work. In such configuration, the optical signal modulation is enabled by coupling modulation, change in the round-trip phase shift and slight variation of its loss. The modulator has two

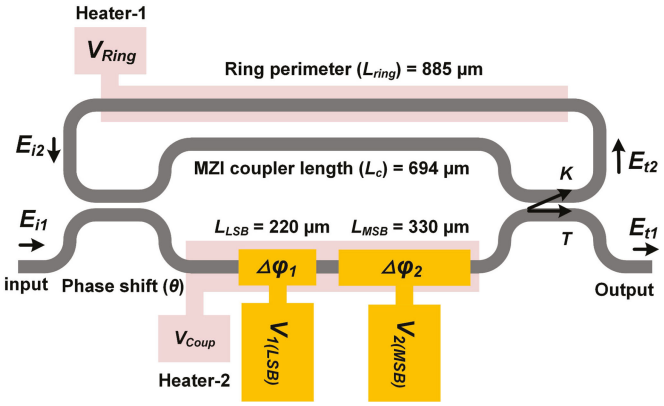

Fig. 3. Schematic of the proposed inter-coupling modulation based PAM-4 ring modulator.

p-n diode segments in the lower arm of the balanced MZI with lengths of $L_{\mathrm{LSB}} = 220\ \mu$m and $L_{\mathrm{MSB}} = 330\ \mu$m. There are also two thermal heaters that were implemented with the top metal layer. The smallest p–n diode segment generates a phase shift $\Delta\phi_1$ with an RF signal V_1 representing the lowest significant bit (LSB). The largest p–n diode segment generates a phase shift $\Delta\phi_2$ with an RF signal V_2 representing the MSB. The heater in the ring (heater-1) is at the top of the cavity to enable a shift in the resonance wavelength so to align it with the laser to modulate. The heater in the lower arm of the MZI (heater-2) generates the required initial phase θ to optimize the extinction ratio and exploit the linear optical transmission portion of the modulator. In this device, the ring cavity length (L_{ring}) and MZI coupling length (L_c) is determined mainly based on the total length of the two p–n diode segments to generate the required phase shift for modulation.

Next, we describe the simulation method used in this work to determine the required length of the two p–n diode segments towards optimal extinction ratio at the targeted reverse bias voltage. Equations (1) and (2) show the transfer matrix and transfer function between the MZI input electric fields (E_{i1} and E_{i2}) and the MZI output electric fields (E_{t1} and E_{t2}) (Fig. 3)

$$\begin{bmatrix} E_{t1} \\ E_{t2} \end{bmatrix} = \begin{bmatrix} T_1 & K_2 \\ K_1 & T_2 \end{bmatrix} \begin{bmatrix} E_{i1} \\ E_{i2} \end{bmatrix} \tag{1}$$

$$E_{i2} = \alpha_{\mathrm{ring}} \exp(-j\delta) E_{t2} \tag{2}$$

where α_{ring} is the total loss, and δ is the phase due to the ring cavity length (L_{ring}) and the effect of heater-1. The matrix elements T_i and K_i representing the transmission from input port i of the MZI to the through-port and cross-port output, respectively ($i = 1, 2$). They are calculated using the following equations:

$$\begin{aligned} T_1 = {} & t_1 t_2 \alpha_{\mathrm{arm1}} \exp(-j(\phi + \Delta\phi_1 + \Delta\phi_2 + \theta)) \\ & + k_1 k_2 \alpha_{\mathrm{arm2}} \exp(-j\phi) \end{aligned} \tag{3}$$

$$\begin{aligned} T_2 = {} & t_1 t_2 \alpha_{\mathrm{arm2}} \exp(-j\phi) \\ & + k_1 k_2 \alpha_{\mathrm{arm1}} \exp(-j(\phi + \Delta\phi_1 + \Delta\phi_2 + \theta)) \end{aligned} \tag{4}$$

$$\begin{aligned} K_1 = {} & k_1 t_2 \alpha_{\mathrm{arm2}} \exp(-j\phi) \\ & + t_1 k_2 \alpha_{\mathrm{arm1}} \exp(-j(\phi + \Delta\phi_1 + \Delta\phi_2 + \theta)) \end{aligned} \tag{5}$$

$$\begin{aligned} K_2 = {} & k_1 t_2 \alpha_{\mathrm{arm1}} \exp(-j(\phi + \Delta\phi_1 + \Delta\phi_2 + \theta)) \\ & + t_1 k_2 \alpha_{\mathrm{arm2}} \exp(-j\phi) \end{aligned} \tag{6}$$

where t_1 and k_1 are the transfer functions of the electric field coupled to the through-port and cross-port of the first directional coupler, respectively, and t_2 and k_2 are the transfer functions of the electric field coupled to the through-port and cross-port of the second directional coupler, respectively. The variable ϕ is the phase due to the MZI coupling length (L_c) and θ is the initial phase generated with thermal heater. For an ideal 50/50 compact directional coupler, $t = 1/\sqrt{2}$ and $k = \exp(-j\pi/2)/\sqrt{2}$, at a specific wavelength. Due to fabrication process variation, however, the coupling coefficient of the directional couplers will differ and considerably affect the performance of the device. The variables α_{arm1} and α_{arm2} are the total losses in the lower and upper arms of the MZI, respectively. The electric field transfer function of the device is calculated from (7):

$$\frac{E_{t1}}{E_{i1}} = \frac{T_1 - (T_1 T_2 - K_1 K_2)\alpha_{\mathrm{ring}} \exp(-j\delta)}{1 - T_2 \alpha_{\mathrm{ring}} \exp(-j\delta)} \tag{7}$$

With the assumption of ideal 50/50 directional couplers and loss-less MZI, the solution to equation (7) leads to the following three equations:

$$T_1 T_2 - K_1 K_2 = \exp(-j(2\phi + \Delta\phi_1 + \Delta\phi_2 + \theta)) \tag{8}$$

$$\begin{aligned} T_1 = {} & \sin((\Delta\phi_1 + \Delta\phi_2 + \theta)/2). \\ & \exp(-j(2\phi + \Delta\phi_1 + \Delta\phi_2 + \theta + \pi)/2) \end{aligned} \tag{9}$$

$$\begin{aligned} T_2 = {} & \sin((\Delta\phi_1 + \Delta\phi_2 + \theta)/2). \\ & \exp(-j(2\phi + \Delta\phi_1 + \Delta\phi_2 + \theta - \pi)/2) \end{aligned} \tag{10}$$

Unlike the inter-coupling ring modulator with push–pull driving signals where the resonance condition depends on the constant phases ($2\phi + \theta + \delta = 2m\pi$, m is integer), the resonance condition for single ended driving signal ($2\phi + \Delta\phi_1 + \Delta\phi_2 + \theta + \delta = 2m\pi$, m is integer) depends on the variation of both phase shifts $\Delta\phi_1$ and $\Delta\phi_2$. Applying an electrical driving signal results in both a shift in the resonance wavelength as well as a change in the transmission amplitude.

To simulate the general behavior of the device for various biasing conditions, we followed the methodology presented in [9]. First, we calculate the variation in the refractive index of the doped silicon in presence of free carriers for various biasing voltages applied to the p–n diode. We then compute the effective refractive index and the corresponding mode profile using the effective index method. The voltage-dependent effective index and loss are calculated based on the mode profiles and charge carrier distributions [10]. Finally, based on the properties and geometry of the device and applied voltage, the electric field transfer function (7) is calculated for various wavelengths and bias voltages. The normalized output transmission

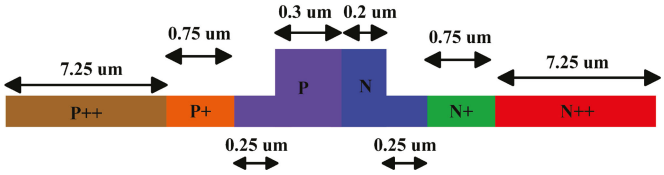

Fig. 4. Cross-section of the p–n diode segment with dimensions for each doping layer.

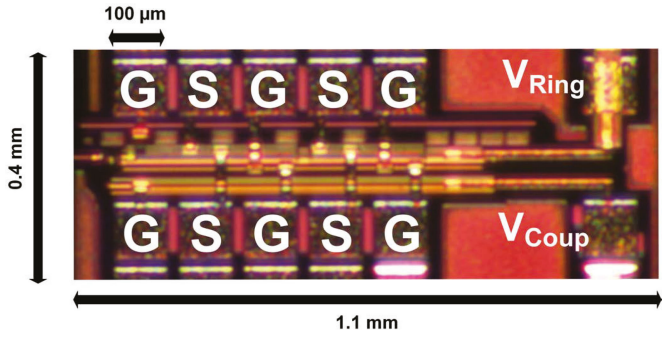

Fig. 5. Microscopic image of the designed ring modulator on chip excluding the optical grating couplers.

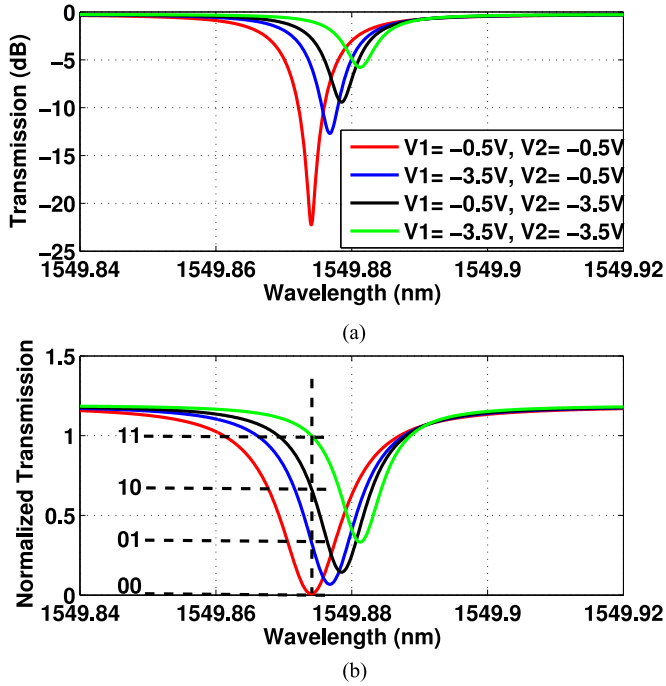

Fig. 6. The simulated spectral response of the modulator at four input voltage conditions, (a) in logarithmic scale, (b) in linear scale.

power is taken as the square of the absolute value obtained using equation (7). Fig. 4 shows the cross-section of the designed p–n diode segments with dimensions for each doping layer, which is used for the simulation. Doping densities were found using Sentaurus Device simulation software for the specific doping dose and doping energy for each doping layer. The average doping densities for the p++, p+, p, n++, n+ and n layers were found to be 1.2×10^{20} cm^{-3}, 1.8×10^{18} cm^{-3}, 4×10^{17} cm^{-3}, 3.3×10^{20} cm^{-3}, 3×10^{18} cm^{-3}, 3.2×10^{17} cm^{-3}, respectively. It should be mentioned that the highly doped p++ and n++ layers were used to form the low resistance contact with the top metal layer. The intermediate doping layers (p+ and n+) were formed to further reduce the series resistance [11]. The intermediate doping layers were 0.25 μm apart from the rib waveguide to minimize the optical propagation loss.

The total length of the p–n diode segments (220 μm and 330 μm) is determined based on the required phase shift for 0 to 1 modulation. In the inter-coupling ring modulator, the required phase shift ($\Delta\phi$) for 0 to 1 modulation is $\Delta\phi_1 = \pi - 2\sin^{-1}\alpha$, where α is the total round trip loss of the resonator cavity ($\alpha = \alpha_{\text{ring}} \times \alpha_{\text{arm1}} \times \alpha_{\text{arm2}}$) [7], [8]. With larger cavity loss (smaller α), more phase shift is required resulting in larger total length of the p–n diode and/or larger applied voltage. For PAM-4 modulation, the length ratio of the longer and shorter p–n diode segments is designed to have four equidistant transmittivity levels for specific bias voltages of the LSB and MSB diode segments. The optimized design of the modulator has a cavity feedback length of $L_{\text{ring}} = 885$ μm and a MZI coupling length of $L_c = 694$ μm. The total design area of the modulator is 0.48 mm^2. The microscopic image of the designed modulator on the chip is shown in Fig. 5. Each of the DC and RF electrical pads has 100 μm $\times$ 100 μm area. In Fig. 5, optical grating couplers (area: 40 μm $\times$ 30 μm) are not shown, as the grating couplers are placed at the edge of the chip.

Fig. 6 shows the simulated spectral response of the designed PAM-4 modulator for four voltage conditions. The propagation loss of the undoped waveguide is considered to be 2 dB/cm. The simulation results show the inter-coupling effect where the resonance extinction ratio is changing for the applied voltages. The cavity phase shift effect on the resonance wavelength for various biasing voltages is also apparent. In this simulation, the initial phase of θ is set to 2.5 rad for optimum extinction ratio and linear performance. Based on the simulation results the free spectral range (FSR) of the design modulator is 0.39 nm.

IV. Experimental Demonstration and Results

In this section, we present the experimental result of the fabricated PAM-4 modulator. Fig. 7(a) shows the characterization test setup of the fabricated modulator with the two DC and two GSGSG RF probes. The DC probes are used to apply DC voltages to the heaters to optimize the ring modulator's extinction ratio (V_{COUP}) and to shift the resonance wavelength (V_{ring}) to match the wavelength of the CW light source. Both the DC signals share common electrical ground (G) with the RF signals. Fig. 7(b) shows photograph of the external fiber array and electrical probe connections to the chip.

To determine the amplitude and DC bias of the electrical driving voltages and the resonance wavelength, a continuous wave (CW) laser source emitting an optical output power of 5 dBm is injected into the modulator. Its wavelength is swept from 1530 to 1565 nm. Fig. 8(a) shows the spectral response of the modulator when the voltage at the thermal tuner/heater on top of the MZI arm is set to 1.2 V (drawn current: 2 mA). The grating coupler (GC) pair transmission response shows around 2 dB insertion loss in the modulator. Fig. 8(b) is a zoom on the

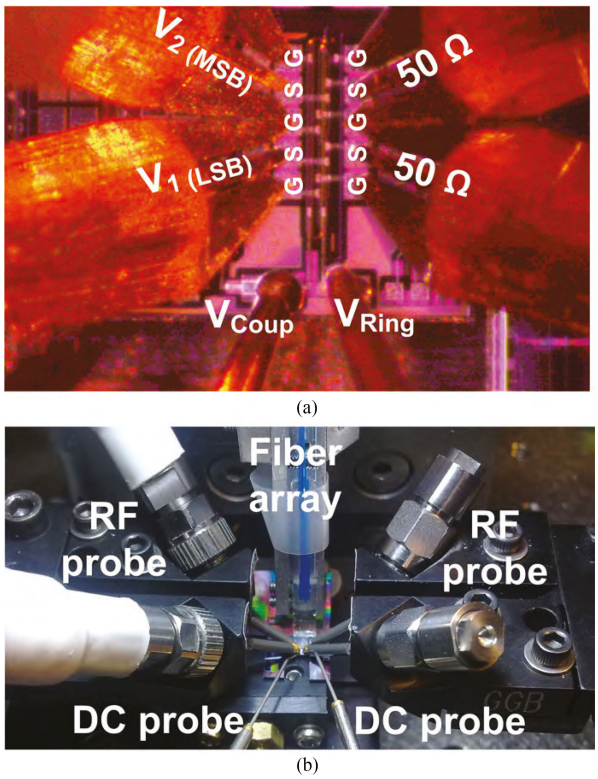

Fig. 7. (a) Image of the chip test setup with DC and RF probes, (b) Test setup photograph of the chip with fiber array and electrical probes.

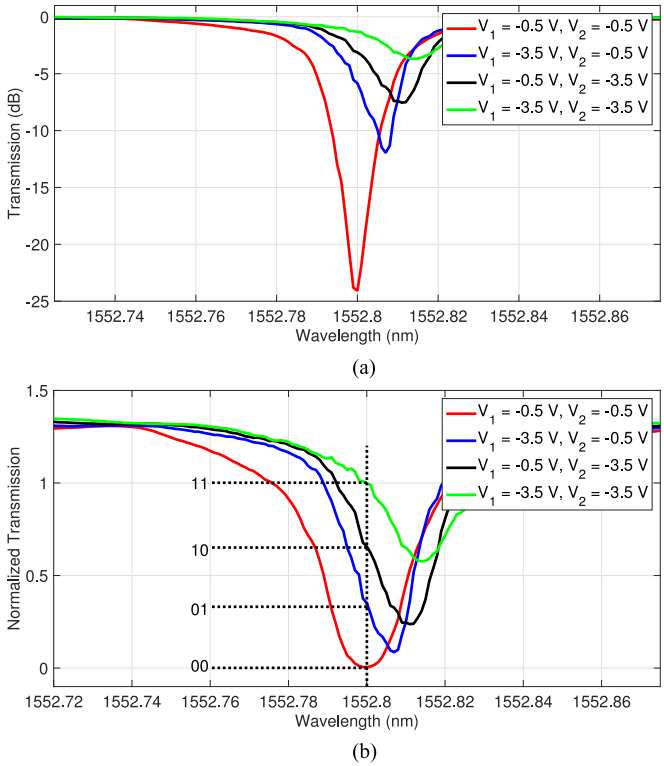

Fig. 9. Measured spectral response of the modulator at four input voltage conditions (a) in dB scale, (b) in linear scale.

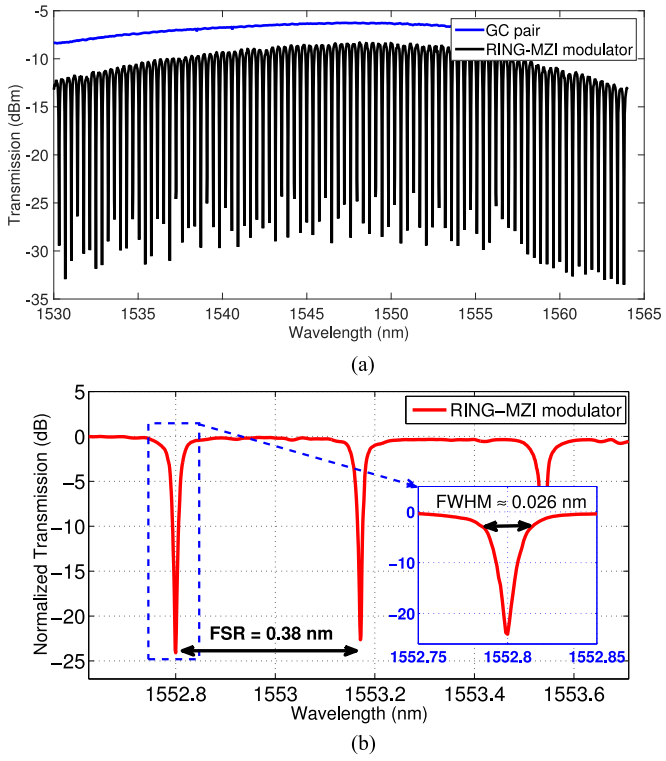

Fig. 8. (a) Spectral response of the GC pair and ring modulator, (b) Spectral response of the modulator (zoomed) to measure FSR, inset: FWHM of approximately 0.026 nm, from the spectral response of the ring modulator.

spectral response of the modulator to measure the FSR of the modulator. From this figure we measure an FSR of 0.38 nm, which is in line with the simulated results of 0.39 nm presented in Section III. Fig. 8(b) also shows the full width at half max (FWHM) linewidth of approximately 0.026 nm at the resonance wavelength $\lambda_0 =$ 1552.8 nm from the spectral response of the modulator. This FWHM corresponds to a relatively high loaded Q factor of 59,720. The Q factor is limited by the increased loss in the ring cavity due to the long p-n diode segments (total p-n diode segment length = 550 μm). Shorter segments would increase the loaded Q factor at the expense of lower extinction ratio in the generated PAM-4 signal.

Fig. 9(a) shows the spectral response of the modulator recorded at 1552.8 nm for four input voltage conditions setting the p–n electrode in reverse bias mode. For all conditions, the fixed DC bias voltage to the thermal tuner/heater is maintained at 1.2 V (drawn current = 2 mA). From this figure, it is seen that while the resonance wavelength shifts, the extinction ratio also diminishes with changes in the applied voltage as expected from simulation of the transmission response of the modulator. This phenomena in inter-coupling based modulator relaxes the voltage condition to achieve four optical levels by reducing the steep slope of the transmission response at the resonance wavelength. From Fig. 9(a), we measure normalized optical power levels of 0, −1.82, −4.63 and −22.75 dB at 1552.8 nm wavelength. In the linear scale (Fig. 9(b)), the four optical power levels correspond to the modulator transmittivity of 1, 0.65, 0.34 and 0.005, respectively. The four equidistant transmittivity values indicate

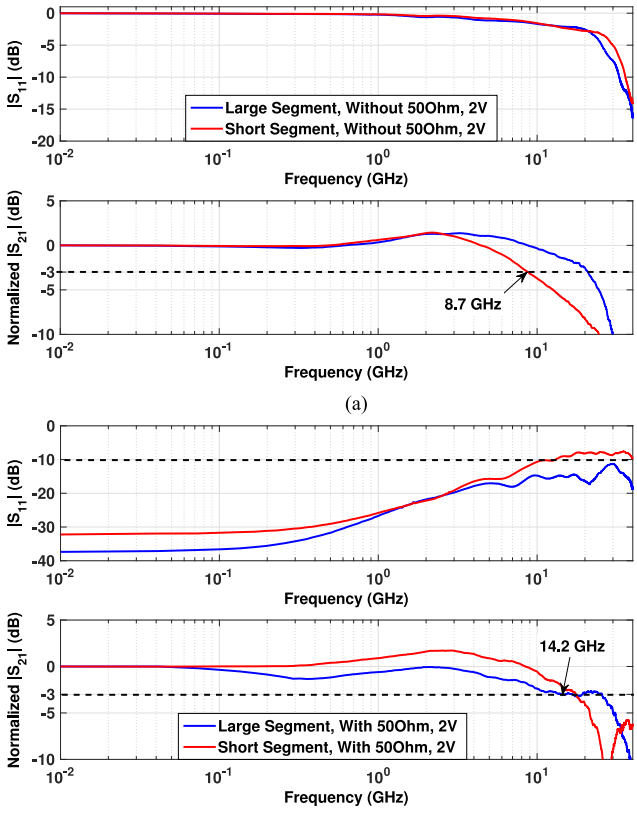

Fig. 10. S-parameter measurements: S_{11}-parameter and EO S_{21}-parameter of the long and short electrodes, (a) without 50 Ω termination, (b) with 50 Ω termination.

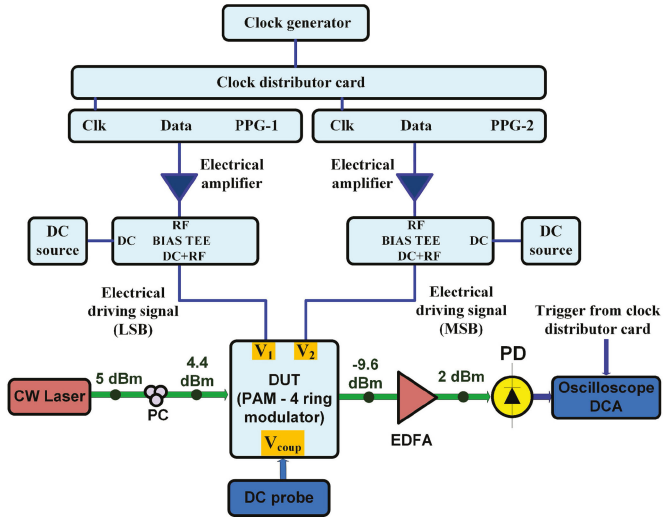

Fig. 11. Experimental setup to generate PAM-4 modulated signal. PPG: pulse pattern generator, EDFA: Erbium doped fiber amplifier, PC: polarization controller, PD: photodetector, DCA: digital communication analyzer.

that the ring modulator can properly generate PAM-4 optical signal at the output when driven by two independent electrical signals.

We perform small signal characterization using a 50 GHz Agilent N5225A lightwave component analyzer, and two 40 GHz GSG probes to evaluate the 3-dB bandwidth of the modulator. We measured the S-parameter of each short and long electrode separately. One of the GSG probe is used on one of the two electrodes with electrical RF signal while another GSG probe is used for the 50 Ω termination of the connected electrode. Fig. 10 shows the S-parameter measurement (input reflection (S_{11}) in the top figure and electro-optic (EO) S_{21} response in the bottom figure) at 2 V reverse bias voltage of the short and long electrode segments with and without connecting a 50 Ω termination. A large reflection is expected without the 50 Ω termination in the S_{11} measurement (Fig. 10(a)-top). The reflection drops after 12 GHz. With a 50 Ω termination, the reflection is reduced to below 20 dB up to 2 GHz and −10 dB at 12 GHz (Fig. 10(b)-top). While the smallest EO bandwidth measured from the S_{21} transmission measurement curves of the p–n diode without the 50 Ω termination is approximately 8.7 GHz, it is worth noting that the high speed modulation is limited by the high reflection. At 2 V reverse bias voltage, both of the electrodes have OE bandwidth over 14 GHz with the 50 Ω termination.

Next, we test the device to generate optical PAM-4 signal. To generate each of the two driving signals, we use two 12.5 Gb/s data rate Anritsu-MU181020A programmable pattern generator (PPG) cards in synchronous mode to tune the phase of each of the electrical driving signal independently. As such, the rising and falling edges of the two input signals occur at the same time. Fig. 11 shows the experimental setup to generate PAM-4 signal from the modulator.

Two independent 2^{31}–1 pseudorandom binary sequences (PRBS) data from two PPGs are injected to two 20 GHz electrical amplifiers (model: Hittite HMC-C004) boosting the signal amplitude to 3 V_{pp} and then be the input to two 6 GHz bias-T to add the desirable DC bias to the driving electrical signal. The DC bias is provided by two DC sources and reverse biased the diode segments. The two RF signal are injected to the LSB and MSB electrode segments of the inter-coupling ring modulator. The subfigure of Fig. 12 shows the electrical eye diagrams of the 12.5 Gb/s driving signals for the MSB and LSB electrode segments, respectively. The bandwidth limitation of the two 6 GHz bias tees and noise injected by the electrical amplifier limits the signal to noise ratio (SNR = 8).

A 5 dBm CW light at the wavelength of 1552.8 nm is launched through the polarization controller (PC) which optimizes the light coupled to the inter-coupling PAM-4 modulator. The average optical power at the output of the modulator is −9.6 dBm. The total optical loss from the laser to the modulator output consists of 0.6 dB insertion loss from the PC, 2 dB insertion loss from the modulator (DUT) and 6 dB loss per grating coupler. The optically modulated signal is amplified with an erbium doped fiber amplifier (EDFA) to increase the received optical signal to 2 dBm at the receiver. A commercial 45 GHz photodetector (PD) converts the optical PAM-4 signal (responsivity: 0.5 A/W). The commercial PD (from Discovery Semiconductors, Inc.) has an optical power sensitivity of 3.5 dBm at 42 Gb/sec data rate. The electrical signal is finally captured with a sampling oscilloscope (DCA) with an RF bandwidth of 30 GHz.

Fig. 12 shows the photodetected electrical eye diagrams from the output of the ring modulator when it is driven by V_1 (LSB)

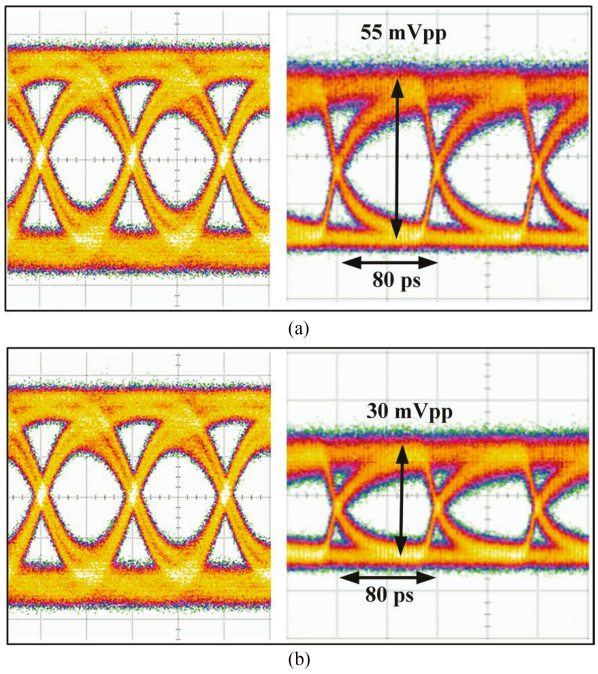

Fig. 12. Eye diagrams (12.5 Gb/s) at the output of the ring modulator when driven by (a) only V_2 (MSB), (b) only V_1 (LSB). The corresponding electrical eye diagrams are shown at the left.

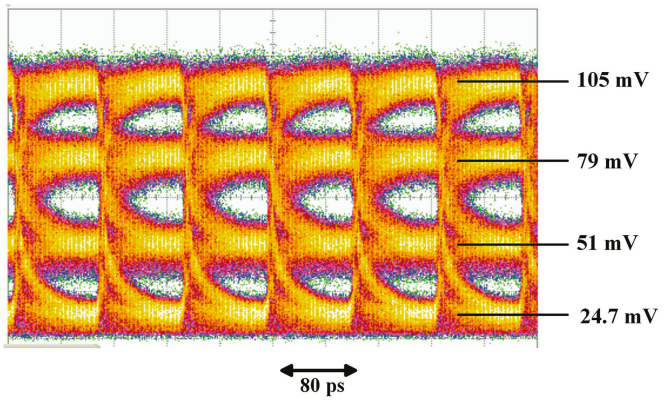

Fig. 13. PAM-4 eye diagram (12.5 GBaud/s) at the output of the ring modulator when simultaneously driven by V_1 (LSB) and V_2 (MSB) electrical driving signals.

and V_2 (MSB), one at a time. The peak-to-peak voltage amplitude of the modulated signal for the shorter p–n diode (V_1) is smaller (approximately half) than that of the longer segment (V_2) as the LSB diode segment (or phase shifter) length is smaller than the MSB segment length. Due to the nonlinear optical response to applied electrical voltage, the length ratio between the LSB and MSB segment is actually not half but 2/3 (220/330 = 0.66).

Fig. 13 shows the photodetected 25 Gb/s PAM-4 electrical eye diagram when the modulator is simultaneously driven by V_1 and V_2. The voltage difference between adjacent levels is approximately 27 mV leading to symmetric four level signal.

We recorded the standard deviation (σ) of the '0' level and '1' level of the OOK eye diagram for both MSB and LSB segments,

TABLE I
THE STANDARD DEVIATION OF THE CAPTURED OOK AND PAM-4 EYE DIAGRAMS

	MSB (OOK)		LSB (OOK)		PAM–4			
level	(0)	(1)	(0)	(1)	(00)	(01)	(10)	(11)
σ (mV)	3.5	4.8	2.5	3.3	4.3	5.2	5.1	5.2

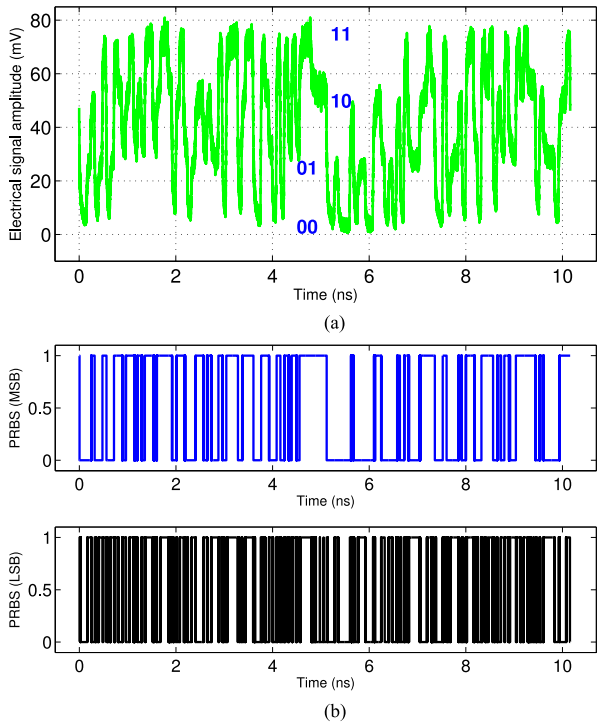

Fig. 14. (a) Pattern locked PAM-4 signal generated. (b) Recovered MSB and LSB patterns from the PAM-4 signal.

and the standard deviation of each four level of the PAM-4 signal. Table I summarized the standard deviation values. The increase in the 'σ' of each of the four levels indicates that there is some crosstalk between the two electrical driving signals.

To verify that the original binary stream of the MSB and LSB OOK data can be properly recovered from the PAM-4 signal, we have captured and store a 2^7-1 PRBS patterned locked data using the sampling oscilloscope. Fig. 14(a) shows the captured PAM-4 signal data stream which was then processed offline in MATLAB to recover the two original MSB and LSB input data. Fig. 14(b) shows the recovered MSB and LSB data. The regenerated data is compared against the original input MSB and LSB data, which shows no error in the modulated data.

We estimated the energy consumption of the modulator by separately calculating the static and dynamic dissipated power. The static power dissipated by the modulator is governed by the two 50 Ω termination loads ($P_{\text{static1}} = 2 \times V_{\text{DC}}^2/50$), where $V_{\text{DC}} = 2$ volt and the thermal heater ($P_{\text{static2}} = V_{\text{th}} \times I_{\text{th}}$), where $V_{\text{th}} = 1.2$ volt, $I_{\text{th}} = 2$ mA. The total static power dissipation of the modulator is 6.5 pJ/bit. We then estimate the dynamic power dissipation of the modulator based on the estimated switching energy ($E_s = CV_{pp}^2$), where C is the para-

sitic capacitance of the diode segment and V_{pp} is the peak-to-peak driving voltage [12]. Based on our simulation results, the short diode segment has a parasitic capacitance of ∼34 fF, and the long diode segment has a parasitic capacitance of ∼51 fF. The estimated dynamic power consumption is 0.0765 pJ/bit and 0.144 pJ/bit for the short and long segment, respectively. It is worth mentioning that practically, the designed modulator can be wire bonded or flipped-chip to a driver. In such configuration, the 50 Ω termination is not required when the driver can be designed for low reflection and optimum power transmission based on the load effect of the diode segments. Therefore, the static power consumption would be mainly limited to the power dissipates by the thermal heater on top of the MZI arm. In fact, using the 50 Ω termination gives us the possibility to test the modulator without the limitation effect of the large reflection.

V. Conclusion

The 12.5 GBaud/s PAM-4 eye diagram obtained by inter-coupling modulation with $3V_{pp}$ electrical driving signal shows promise towards the design of a power efficient optical modulator with small footprint of 0.48 mm^2. We have demonstrated reverse bias operation of the MZI assisted ring modulator which enables generating PAM-4 signal with the conventional on–off keying electrical driving signal. A test methodology was also presented to generate four level optical signals by tuning the extinction ratio of the device using DC heater. The heater layers on top of the waveguide demonstrated in this work introduce less optical waveguide loss (under 2 dB insertion loss) than the conventional heavily doped heaters. Driving the modulator with single drive electrical signal further reduces the operation complexity of the modulator.

The experimental values of the optical powers levels and FSR of the modulator closely agree with the simulation results presented in this work. The availability of tunable directional couplers in silicon photonics [13], enables more robust MZI assisted ring modulator by achieving an exact 3 dB coupling ratio in the MZI. This may facilitate the balanced operation of the MZI through a more robust design to process variation achieving higher data rates in a push–pull PAM-4 modulator configuration.

Acknowldgement

The authors acknowledge the contribution and technical support of CMC Microsystems. The device was fabricated at IME-A*Star in Singapore.

References

[1] N. Kikuchi and R. Hirai, "Intensity-modulated/direct-detection (IM/DD) Nyquist pulse-amplitude modulation (PAM) signaling for 100-Gbit/s/λ optical short-reach transmission," in *Proc. Eur. Conf. Opt. Commun.*, Sep. 2014, pp. 1–3.

[2] X. Wu *et al.*, "A 20Gb/s NRZ/PAM–4 1V transmitter in 40 nm CMOS driving a Si-photonic Modulator in 0.13 μm CMOS," in *Proc. IEEE Int. Solid-State Circuits Conf.*, Feb. 2013, pp. 128–129.

[3] R. Dubé-Demers, C. S. Park, S. LaRochelle, and W. Shi, "60 Gb/s PAM–4 operation with a silicon microring modulator," in *Proc. 12th IEEE Int. Conf. Group IV Photon.*, Aug. 2015, pp. 153–154.

[4] M. S. Hai, M. M. P. Fard, and O. Liboiron-Ladouceur, "A low-voltage PAM–4 SOI ring-based modulator," in *Proc. IEEE Photon. Conf.*, Oct. 2014, pp. 194–195.

[5] W. Sacher *et al.*, "Coupling modulation of microrings at rates beyond the linewidth limit," *Opt. Express*, vol. 21, no. 8, pp. 9722–9733, Apr. 2013.

[6] Q. Xu, B. Schmidt, S. Pradhan, and M. Lipson, "Micrometre–scale silicon electro–optic modulator," *Nature*, vol. 435, no. 7040, pp. 325–327, May 2005.

[7] S. Karimelahi and A. Sheikholeslami, "PAM-N signaling by coupling modulation in a ring resonator," *Opt. Lett.*, vol. 40, no. 3, pp. 332–335, Feb. 2015.

[8] A. Yariv, "Critical coupling and its control in optical waveguide–ring resonator systems," *IEEE Photon. Technol. Lett.*, vol. 14, no. 4, pp. 483–485, Apr. 2002.

[9] L. Chrostowski and M. Hochberg, *Silicon Photonics Design: From Devices to Systems*. Cambridge, U.K.: Cambridge Univ. Press, 2015.

[10] R. Dubé-Demers *et al.*, "Analytical modeling of silicon microring and microdisk modulators with electrical and optical dynamics," *J. Lightw. Technol.*, vol. 33, no. 20, pp. 4240–4252, Oct. 2015.

[11] M. Streshinsky *et al.*, "Low power 50 Gb/s silicon traveling wave Mach–Zehnder modulator near 1300 nm," *Opt. Express*, vol. 21, no. 25, pp. 30350–30357, Nov. 2013.

[12] E. Timurdogan *et al.*, "An ultralow power athermal silicon modulator," *Nature Commun.*, vol. 5, no. 4008, pp. 1–11, Jun. 2014.

[13] P. Orlandi *et al.*, "Tunable silicon photonics directional coupler driven by a transverse temperature gradient," *Opt. Lett.*, vol. 38, no. 6, pp. 863–865, Mar. 2013.

Mohammed Shafiqul Hai received the B.Sc. degree in electrical and electronic engineering from the Bangladesh University of Engineering and Technology, Dhaka, Bangladesh, in 2007 and the M.Eng. (Thesis) degree in electrical engineering from McGill University, Montreal, Canada, in 2011. He is currently working toward the Ph.D. degree at the Department of Electrical and Computer Engineering, McGill University, Montreal, Canada. His research interests include modeling and characterization of nanophotonic devices on silicon on insulator, InP, and Si_3N_4 platforms and components for next generation optical fiber and RF communication.

Monireh Moayedi Pour Fard (S'12) received the B.S. and M.S. degrees in electrical engineering from the K. N. Toosi University of Technology, Tehran, Iran, in 2006 and 2009, respectively. She is currently working toward the Ph.D. degree in electrical engineering at the Photonic Systems Group, McGill University, Montreal, QC, Canada. Her research interests include power–efficient optical systems, electronic and photonic integrated circuits, and photonic interconnects.

Odile Liboiron-Ladouceur (M'95–SM'14) received the B.Eng. degree in electrical engineering from McGill University, Montreal, QC, Canada, in 1999, and the M.S. and Ph.D. degrees in electrical engineering from Columbia University, New York, NY, USA, in 2003 and 2007, respectively. She is currently an Associate Professor and Canada Research Chair in Photonics Interconnect at the Department of Electrical and Computer Engineering, McGill University. Her research interests include optical systems, photonic integrated circuits, and photonic interconnects. She is the author or coauthor of more than 40 papers in peer-reviewed journals and 85 papers in conference proceedings.